



Microstructure and Mechanical Properties of the Plasma-Sprayed and Cold-Sprayed $\text{Al}_{0.5}\text{CoCrFeNi}_2\text{Ti}_{0.5}$ High-Entropy Alloy Coatings

Rotich Sammy Kiplangat¹ · Tzu-Tang Lin¹ · Ngetich Gilbert Kipkirui¹ · Shih-Hsun Chen^{1,2}

Submitted: 16 September 2021 / in revised form: 22 December 2021 / Accepted: 3 February 2022 / Published online: 24 February 2022
© ASM International 2022

Abstract In this study, $\text{Al}_{0.5}\text{CoCrFeNi}_2\text{Ti}_{0.5}$ high-entropy alloy (HEA) powders were prepared by the gas atomization method. The sieved powders with particle sizes of 10–60 and 60–120 μm gas-atomized powders were chosen for further analysis and coatings' application processes. The as-obtained powders possessed spherical shape and uniform element distribution with an initial FCC structure with a minor BCC phase. The as-atomized powders were annealed at 1000 °C temperature for varying durations and characterized to determine their stable state properties. After annealed at 10000 °C, the metastable BCC phase disappeared and $\text{Al}_{0.5}\text{CoCrFeNi}_2\text{Ti}_{0.5}$ transformed into solid-solution FCC matrix with minor BCC precipitates. The Vickers hardness of the plasma-sprayed coatings showed an increasing trend from 285.3 to 396.7 HV as the current was raised from 500 to 750 A, respectively. Cold-sprayed coatings were performed on both carbon steel and aluminum alloy AA 6061, and their properties were

analyzed. The obtained hardness of 426.6 HV was about 10% higher than the plasma-sprayed coatings. Plasma-sprayed coating properties can be varied with plasma power and size of the powder particles. Mechanical locking effect enhanced the bond strength in cold-sprayed AA 6061 compared to carbon substrate. Improved mechanical properties in this alloy were due to precipitation hardening after titanium addition.

Keywords $\text{Al}_{0.5}\text{CoCrFeNi}_2\text{Ti}_{0.5}$ · annealing · gas atomization · HEAs · microstructure · plasma-sprayed · precipitation hardening

Introduction

High-entropy alloys (HEAs) are formed by combining five or more elements together to form a simple solid solution either in equal or near equiatomic ratios. Because of a higher entropy, HEAs present a more stable state and commonly appear in one or two basic crystal structures, e.g., face-centered cubic (FCC) or body-centered cubic (BCC). The high-entropy effect in HEAs results from mutual solubility of constituent elements (Ref 1). The characteristics of HEAs are contrary to the traditional alloy system and are defined by the competition or coupling of two or more compositions. This impacts HEAs with some particular properties, such as high strength, ductility, low diffusion rate, corrosion, and wear resistance, and thus attracts considerable interests from the academia and the industry (Ref 2). Engineers and scientists have been investigating ways on how to harness some of the benefits of HEAs for industrial applications. Notably, AlCoCrFeNi combination of alloys has been widely researched through

This article is part of a special topical focus in the Journal of Thermal Spray Technology on High Entropy Alloy and Bulk Metallic Glass Coatings. The issue was organized by Dr. Andrew S.M. Ang, Swinburne University of Technology; Prof. B.S. Murty, Indian Institute of Technology Hyderabad; Distinguished Prof. Jien-Wei Yeh, National Tsing Hua University; Prof. Paul Munroe, University of New South Wales; Distinguished Prof. Christopher C. Berndt, Swinburne University of Technology. The issue organizers were mentored by Emeritus Prof. S. Ranganathan, Indian Institute of Sciences.

✉ Shih-Hsun Chen
shchen@mail.ntust.edu.tw

¹ Department of Mechanical Engineering, National Taiwan University of Science and Technology, Taipei 10607, Taiwan

² High Entropy Materials Center, National Tsing Hua University, Hsinchu 30013, Taiwan

different processing routes and their properties were extensively analyzed (Ref 3–8).

Cheng et al. (Ref 7) reported that the phase constitution of AlCoCrFeNi coatings was of BCC/FCC dual structure and its phase would be varied with spraying parameters and the powder size. High Al contents promote the formation of BCC structure while reducing the Al amount leading to the formation of FCC structure (Ref 9). Moreover, increasing the Ni content in AlCoCrFeNi promotes the formation of an FCC phase (Ref 10). Continuous phase change of AlCoCrFeNi is not suited to work at elevated temperatures. It is possible to achieve better combination of properties in AlCoCrFeNi by controlling its elemental composition. The Al_{0.5}CoCrFeNi₂ was reported to have good phase stability when annealed and retained the same phase during the thermal spray process and the hardness of plasma coating increased with increasing current and argon gas flow (Ref 8).

The addition of Ti to the AlCoCrFeNi increases the hardness and corrosion resistance of AlCoCrFeNi HEA (Ref 11–13). Ti with larger atomic radius causes lattice distortion energy to increase as it occupies lattice sites enhancing solid solution strengthening of the alloy (Ref 14). The wear behavior of Co_{1.5}CrFeNi_{1.5}Ti and Al_{0.2}-Co_{1.5}CrFeNi_{1.5}Ti was found to be higher than that of conventional wear-resistant steels possessing similar hardness. However, the formation of intermetallic phases has been reported when higher contents of Ti are added (Ref 15). Due to high strength and wear resistance, AlCoCrFeNiTi_x HEAs are great candidates for application in surface technologies to improve surface properties of substrates. Despite the many benefits, HEAs application has been difficult and challenging.

The sluggish diffusion rate caused by element competing effect in HEAs bulk results in severe defects, segregation, and other negative impacts to its characteristics (Ref 2). This leads to high production cost for high-quality HEA bulk and curtails their practical applications. Previous studies (Ref 7, 8, 16) have shown that producing gas-atomized powders by controlling the cooling rate deters long-range segregation to achieve uniform composition and distribution. Numerous methods have been explored in HEAs' powder production with gas atomization and high-energy ball milling, being among the frequently used methods. Compared to ball milling, gas atomization produces powders with spherical shapes, specific particle size distribution and uniform chemical distribution (Ref 7, 8, 17). With mechanical alloying, varying processing times lead to different product properties caused by impact energy (Ref 14, 18, 19). Furthermore, gas atomization

process is a common industrial process for large-scale powder production that can be applied in rapid surface coating technologies, such as atmospheric plasma spray, cold spray, and 3D printing (Ref 17).

Surface coatings offer the functional protection against aggressive environmental conditions, such as high temperature, wear, corrosion and abrasion. HEAs are considered to be great candidates in surface coating applications due to their excellent properties. Plasma cladding, laser cladding, magnetron sputtering and plasma spraying have been used to produce HEA coatings (Ref 4, 6–8, 14, 18, 19). The above-mentioned processes are fusion-based, and melting of feedstock would be involved at working. During melting and solidification, the element segregation in coatings drives HEAs away from the desired properties. Therefore, it is imperative to explore non-fusion-based technologies that are devoid of the HEA's phase transformation during the depositing process.

Cold-spraying (CS) technology is an emerging solid-state technology, which allows the micron-sized powder to remain in the solid state during the deposition process (Ref 20). The powders are accelerated by a supersonic jet triggered through a converging-diverging nozzle and sprayed onto the substrate to create high-quality dense coating (Ref 20–22). Due to low processing temperature, CS allows for avoidance of defects commonly encountered in high-temperature deposition processes, such as oxidation, and other undesired effects that arise out of plasma-sprayed (PS) coatings. Contrary to thermal spray technology, the particles adhere to the substrate due to kinetic energy of sprayed particles upon impact (Ref 23–25). Cold spraying has been successfully deployed to deposit different metal-based materials such as metals, metal matrix composites and alloys (Ref 23, 26–28) suggesting greater potential in HEAs application. A few studies were reported on cold-sprayed HEA coatings, (Ref 21–23) in which irregular mechanical alloyed powders were used to produce the coatings.

In this study, gas-atomized Al_{0.5}CoCrFeNi₂Ti_{0.5} were prepared and their properties were investigated by annealing at 1000 °C at varying durations to determine their stable state. For the first time, the cold spray was used to produce Al_{0.5}CoCrFeNi₂Ti_{0.5} coating using gas-atomized powders, and the properties would be compared to plasma-sprayed coatings. The phase constitution, chemical composition and mechanical properties of these two processes were analyzed through x-ray diffraction, scanning electron microscopy (SEM, JEOL JSM-7900F), energy-dispersive spectrum (EDS, Oxford Instruments Ultim Max), nanoindenter (Bruker Hysitron TI 980 TriboIndenter) and Vickers microhardness tester.

Table 1 Parameters of plasma-spraying process

Sample	Plasma setup				Spray distance, mm	Relative traversing speed, mm/s	Pitch (mm)	Powder feed rate, g/min	Spray pass
	Current (A)	Ar (l/min)	Voltage (V)	H ₂ (l/min)					
i-500-35	500	35	70.0 ^a	9.3	140	750	5	30	10
i-500-50	500	50							
i-600-35	600	35							
i-600-50	600	50							
i-700-35	700	35							
i-700-50	700	50							
i-750-50	750	50							
ii-500-50	500	50							
ii-700-50	700	50							
ii-700-35	700	35							

(i) and (ii) are denoted as 10-60 and 60-120 μm powders, respectively.

^aThe average voltage is displayed here. Voltage of the plasma-sprayed process varies with currents.

Experimental Procedures

Preparation of Al_{0.5}CoCrFeNi₂Ti_{0.5} Powders

Al_{0.5}CoCrFeNi₂Ti_{0.5} HEA powders were prepared from commercial pure elements with a purity above 99.9%. Based on the designed composition ratio, raw Al, Co, Cr, Fe, Ni and Ti slugs were melted in a high-frequency induction furnace in an argon atmosphere so as to limit oxidation. When passed through the gas nozzle, the homogenous Al_{0.5}CoCrFeNi₂Ti_{0.5} HEA melt was pulverized by the high-pressure argon gas stream and cooled rapidly. The gas nozzle is heated to 700 °C to preserve the smooth atomization of the powders. The collected powders at the bottom of the chamber exhibit a spherical shape and then were sieved into different categories, 10-60 μm and 60-120 μm , which were selected for this study. In this study, the 10-60 μm will be referred as group (i) and 60-120 μm as group (ii). The annealing was done at 1000 °C so as to avoid the formation of intermetallics (σ phase), while the annealing time was varied to study its impact on the precipitates formed.

The powders were annealed at 1000 °C for 2 to 12 hrs. The characterization was carried out on the as-obtained and

annealed powders to evaluate the changes in microstructure and mechanical properties after annealed at 1000 °C for 2 to 12 hrs.

Preparation of Plasma-Sprayed Al_{0.5}CoCrFeNi₂Ti_{0.5} Coatings

The Unicoat APS system with a F4MB90-XL plasma gun (Oerlikon Metco, Switzerland) was used to create Al_{0.5}CoCrFeNi₂Ti_{0.5} coatings on a 5 × 5 × 0.3 cm³ carbon steel substrate. Before the spraying process, the substrate was blasted with alumina to establish a rough surface. To avoid contamination and remove dust, the substrate was further ultrasonically cleaned in ethanol and kept in the oven at 70 °C. Table 1 shows the parameters that were adopted in this study. The coating's microstructure, chemical and physical, and ultimate bonding strengths were examined by adjusting power input in a fixed voltage mode. The thickness of coatings was determined by the number of spray passes, which was generally between 15 and 20 μm per pass. The influences of the particle sizes, the specific input power and the argon gas flow rate on the microstructure and the mechanical properties of the coating were investigated.

Table 2 Parameters of cold-spraying process

Spraying			Feedstock			Robotic arm condition			Substrate preheating, °C
pressure, MPa	Temp, °C	Distance, mm	Pressure, MPa	Gas flowrate, SLM	Feed rate, g/min	Pitch, mm	Linear velocity, mm/sec	Incident angle, °	
5	1000	30	5	300	25.55	0.5	1.56	90	105

The spraying route was maintained at 90° by a plasma gun that was mounted on a robotic arm, which additionally kept the spraying distance constant. Argon and hydrogen were used as the primary and secondary gas, respectively, while nitrogen acted as the carrier gas for the HEAs powder to the plasma gun from the feeder unit. The substrates were kept below 100 °C during the spraying process by three auxiliary jets, which removed the unmelted and weakly bonded powder particles (Ref 8).

Preparation of Cold-Sprayed Al_{0.5}CoCrFeNi₂Ti_{0.5} Coatings

The parameters in Table 2 were adopted in cold spray process using a high-pressure cold spray system equipped with the standard water-cooled de-Laval-type converging nozzle and nitrogen as the carrier gas at a feed rate of 300 SLM. The hard carbon steel (~160 HV) and soft AA 6061 (~107 HV) substrates both measuring 5 × 5 × 0.3 cm³ and 5 × 5 × 0.5 cm³ were sand-blasted prior to cold deposition process. The gas pressure and temperature used during cold spray were 5 MPa and 1000 °C, respectively, while keeping the spray angle of the robotic arm 90°.

Microstructural Characterization

The microstructures of the as-obtained, annealed powders and the coatings were observed using the FE-SEM (JEOL, JSM 7900F), which was equipped with energy-dispersive spectroscopy (EDS) and electron backscattered diffraction (EBSD). Sequentially, the EDS was used to obtain elemental mappings and chemical compositions. EBSD was used to characterize the phase mapping of the annealed powders. Crystallinity of powders and coatings was characterized using the x-ray diffractometer (XRD, Bruker D8) with CuK α radiation ($\lambda = 0.154$ nm).

Mechanical Characterization

Nanoindenter (TI-980, TriboIndenter, Hysitron, USA) was used for nanoindentation of the annealed and as-atomized powders, applying a load of 3 μ N. The load function for nanoindentation is 5 × 5 × 5 mode, which means taking 5 s to increase the load to 3 μ N, holding for 5 s, and then

reducing to zero in another 5 s. Vickers microhardness tester (Akashi MVK-H1) was used to perform hardness testing on the cross-section of the coatings under a load of 0.3 kg with the dwell time set to 15 s. The mean Vickers hardness values were calculated from ten measurements taken on the cross section of each coating sample.

Adhesion test for both the cold-sprayed carbon steel and AA 6061 was performed on a tensile rig as described in the standard test method ASTM C 633 (Ref 28). The tensile load was applied to the disk-shaped slugs at constant rate of 1 mm/s and the amount of force at the point of fracture or separation was recorded. Adhesive strength of epoxy resin is generally not higher than 70 MPa. This restricts coatings with higher adhesion strength than that of the epoxy resin.

Results and Discussion

Characterizations of the Al_{0.5}CoCrFeNi₂Ti_{0.5} HEA Powders

The characterizations of as-atomized Al_{0.5}CoCrFeNi₂Ti_{0.5} powder categorized into two groups as outlined above were performed to study the initial status of the microstructure, crystallinity and the chemical composition. Figure 1(a) and (b) displays the SEM images showing the highly spherical nature of the as-obtained group (i) and (ii) powder suggesting gas-atomization powders of identical size, spherical shape and uniform size distribution (Ref 7, 8, 16, 29). The groups (i) and (ii) as-atomized powder sizes were selected for characterization to understand their initial status. The obvious difference observed in the microstructure of the as-atomized powders is that group (ii) powders had larger precipitates compared to group (i) powders. EDS analysis for group (i) powder was examined on the cross-sectional SEM image as shown in Fig. 1(e). The (Al, Ti) tends to partition forming precipitates, which brings about deviation in composition as demonstrated in Table 3. The results of both groups display the composition slightly varying from nominal design of the Al_{0.5}CoCrFeNi₂Ti_{0.5} HEA. The unmarked peaks in Fig. 1(e) are from the platinum signal applied to enhance the conductivity of the sample in SEM.

Elemental mapping was studied to check the compositional distribution of the elements as shown in Fig. 2(a) and

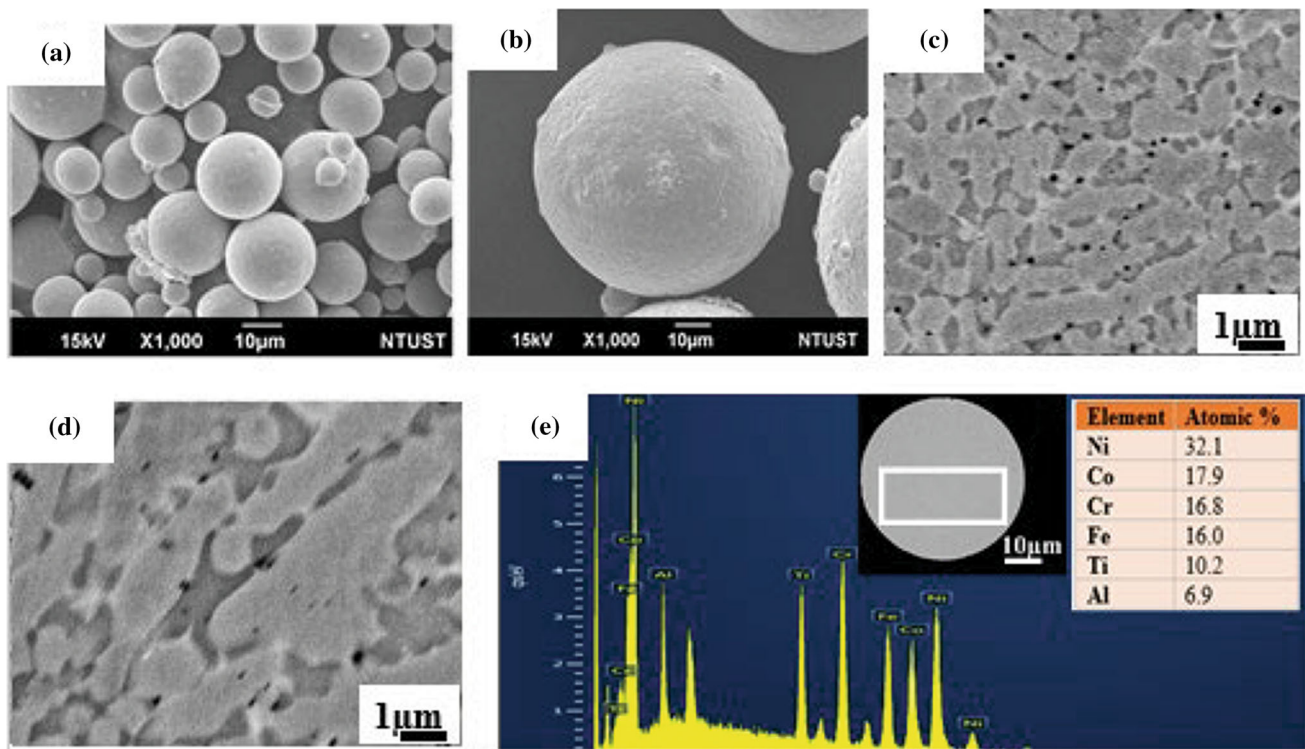


Fig. 1 SEM images showing the morphology and size distribution of as-prepared $Al_{0.5}CoCrFeNi_2Ti_{0.5}$ powders in (a, b) for group (i) and (ii), respectively, the cross-sectional images of group (i), and (ii) in (c) and (d), (e) EDS spectrum of group (i) powder in the selected area

Table 3 The compositions of the designed and as-atomized $Al_{0.5}CoCrFeNi_2Ti_{0.5}$ powders

Element	Composition ratio in at. %					
	Al	Co	Cr	Fe	Ni	Ti
Nominal	8.3	16.7	16.7	16.7	33.3	8.3
Group (i)	6.9	17.9	16.8	16.0	32.1	10.2
Group (ii)	7.5	17.3	16.8	16.5	31.4	10.3

(b). In group (i) powders, an equal distribution of the elements in all the phases depicted in the EDS mapping in Fig. 2(a). However, Fig. 2(b) indicates a clear evidence of segregation in the as-atomized group (ii) powders as the different phase constitutions marked as A and B. From the analysis of the EDS mapping, region A is enriched in Ti and Al, while region B is enriched in Fe and Cr. The Co and Ni are evenly distributed across both regions. EDS point analysis of region A and B shown in Table 4 confirms that the phase contrast in A is enriched in Al and Ti, while region B is enriched in Fe and Cr in group (i) powder. However, the EDS point analysis showed a slight variation of element concentration in regions A and B of group (ii) powder. Region had a higher concentration of Ti and Ni, while region B was enriched in Fe and Cr. Compared to the group (ii) powders, the group (i) powders experienced a

more rapid cooling process which suppressed atomic diffusion and resulted in an even distribution for all the six elements (Ref 7, 8, 29). Smaller-sized droplets have higher velocities during gas atomization as they lack the ability to resist drag forces, which leads to rapid cooling (Ref 14).

Because of the difference of group (i) and (ii) powders in microstructure, further annealing process was conducted on the group (i) powder samples to study the phase stability at 1000 °C for 2, 6 and 12 hrs in a vacuum furnace. Figure 3 shows the XRD spectra of the as-atomized and the annealed group (i) powders. The as-atomized $Al_{0.5}CoCrFeNi_2Ti_{0.5}$ powder was composed of the FCC matrix as the main phase and a metastable BCC phase along (111) and (110), respectively (Ref 8). After annealing at 1000 °C, the metastable BCC peak at 43.995 ° transformed into ordered BCC at 30.549°, disordered BCC peaks intensity at 64.633° and 81.817° increased and the FCC peak became dominant phase due to increased FCC precipitate (Ref 30).

While fast-cooling suppressed the growth of BCC phase along (200) and (211), the annealed powder got sufficient energy to reach their stable state as shown in the XRD spectra in Fig. 3. The dark phases are (Al, Ti)-rich phases as the bright areas are enriched in (Fe, Cr). Both Ti and Al are BCC stabilizers, and thus, the addition of Ti to $Al_{0.5}CoCrFeNi_2$ (Ref 29), which was purely FCC, brought about the precipitation of a BCC phase in $Al_{0.5}CoCrFeNi_2Ti_{0.5}$. As the annealing time increased from 2 hrs to 12 hrs, for

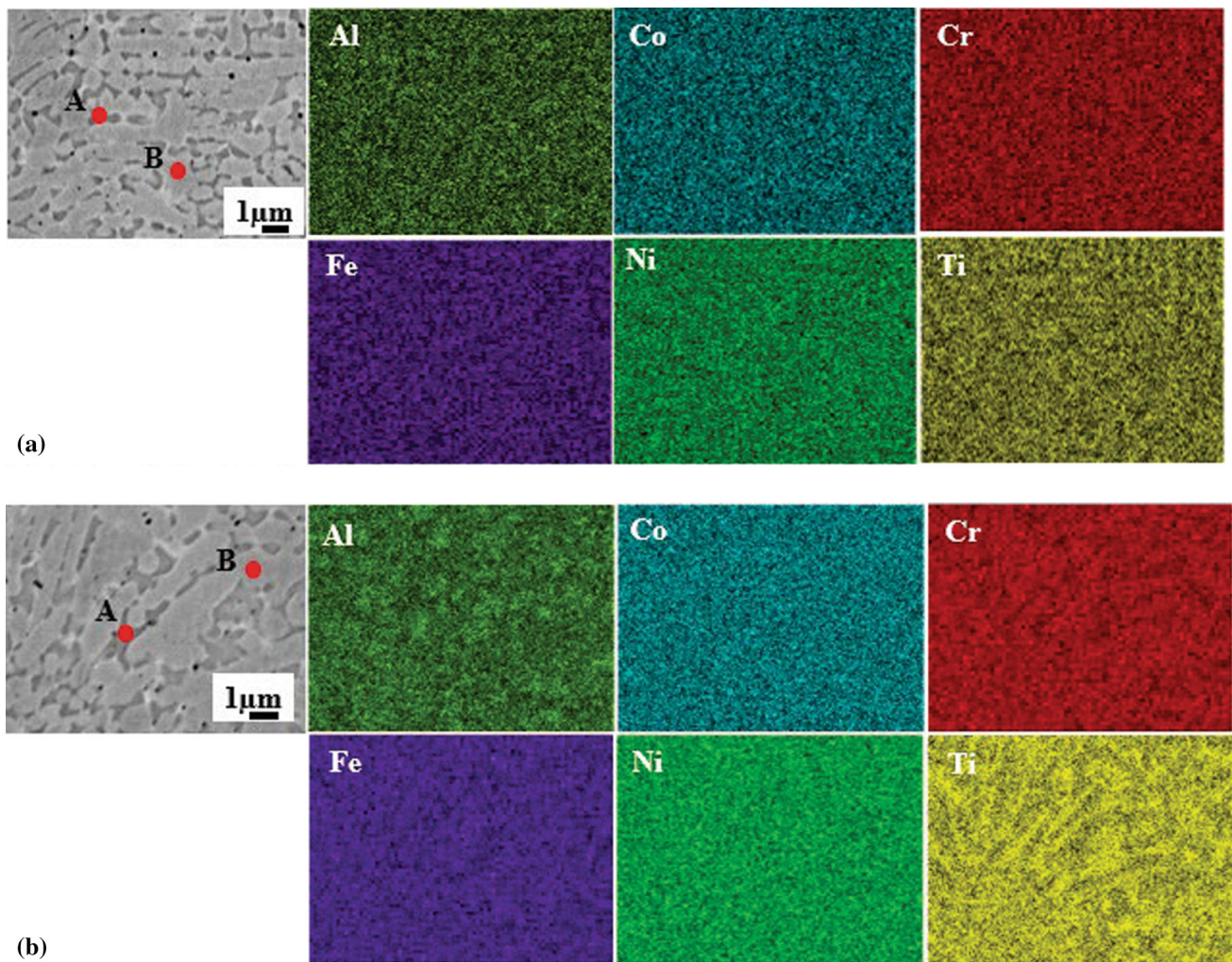


Fig. 2 Backscattered electron diffraction (BSED) image showing the microstructure of the $\text{Al}_{0.5}\text{CoCrFeNi}_2\text{Ti}_{0.5}$ alloy and the phase compositions identified via EDS of (a) group (i) and (b) group (ii) as-atomized powders

Table 4 Point EDS compositions of the group (i) and (ii) as-atomized $\text{Al}_{0.5}\text{CoCrFeNi}_2\text{Ti}_{0.5}$ powders in regions A and B

		Composition ratio in At.%					
Element		Al	Cr	Co	Fe	Ni	Ti
Group (i)	A	10.4	14.3	16.7	14.4	31.5	12.7
	B	7.1	18.5	17.1	17.8	31.8	7.7
Group (ii)	A	6.8	12.8	19.0	13.8	36.3	11.3
	B	3.7	18.6	19.7	18.6	33.3	6.1

the 10–60 μm powders there was no noticeable increase in the BCC precipitates. After 2 hrs of annealing, the microstructure of group (i) was in a stable state and no observable difference as compared with 12-hr annealed powder in Fig. 4(a) and (b). This indicates that the group (i) microstructure attains a stable state after 2 hrs of

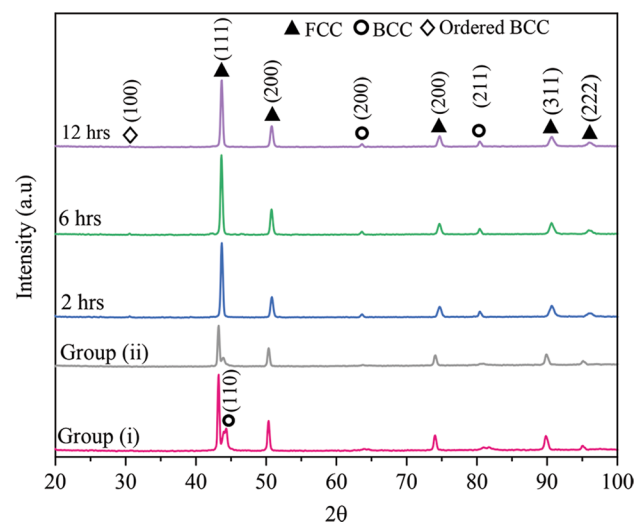


Fig. 3 The XRD spectra of $\text{Al}_{0.5}\text{CoCrFeNi}_2\text{Ti}_{0.5}$ as-atomized and annealed group (i) powders at 1000 °C in different durations

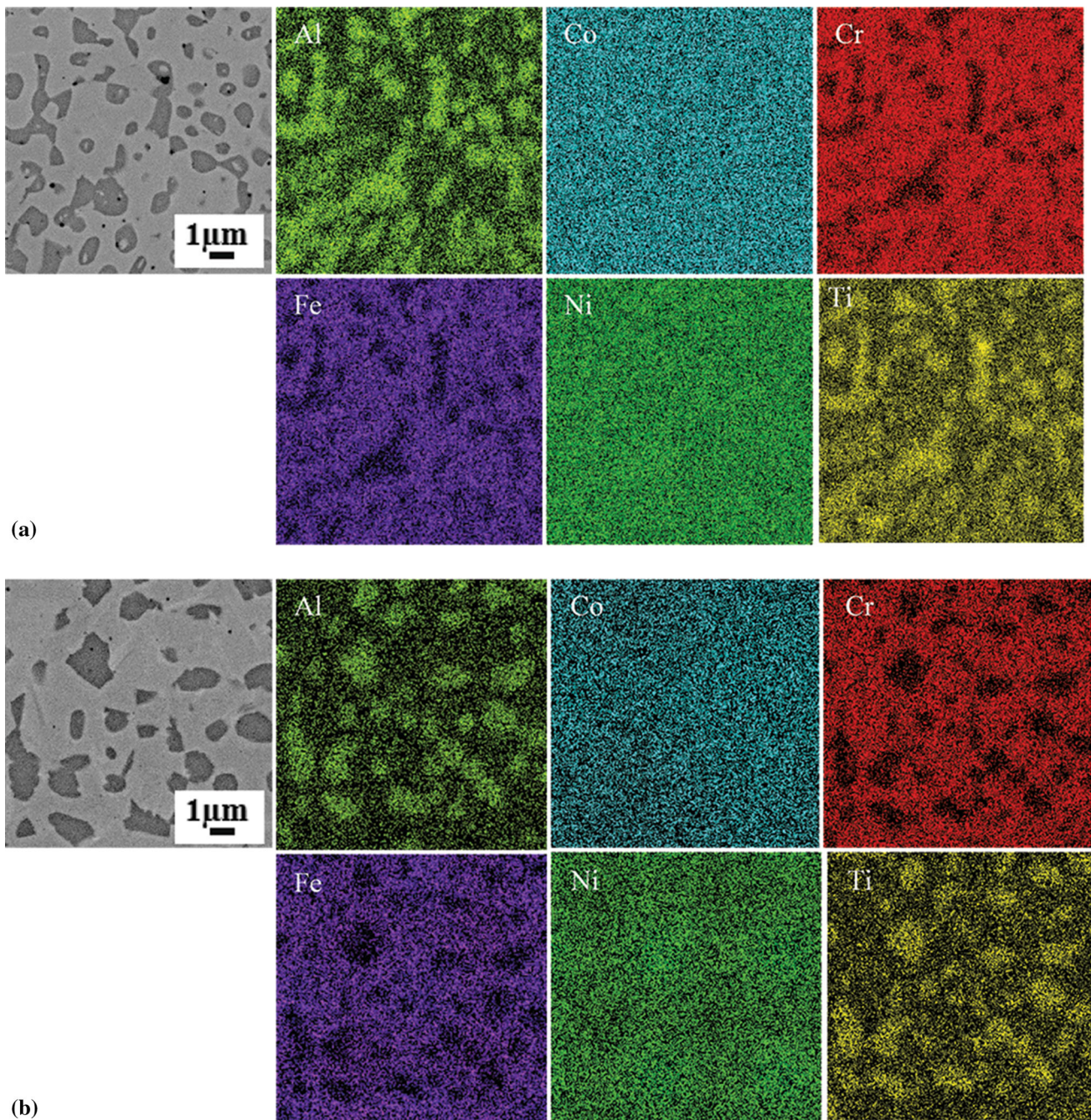


Fig. 4 Elemental mapping of $\text{Al}_{0.5}\text{CoCrFeNi}_2\text{Ti}_{0.5}$ group (i) powders after annealed at 1000 °C for (a) 2 and (b) 12 hrs, respectively

annealing, which may not be affected by high temperatures thereafter.

The new peaks observed in the XRD results after annealed for 2 hrs and 12 hrs necessitated further investigation by phase mapping and analysis of crystal orientation using electron backscattered diffraction (EBSD). The EDS mapping performed on the $\text{Al}_{0.5}\text{CoCrFeNi}_2\text{Ti}_{0.5}$ group (i) powder sample after annealed for 12 hrs demonstrated the evidence of segregation of the Al, Ti, as shown in Fig. 4(b). The band contrast image in Fig. 5(a) shows

distinct grain boundaries of the polycrystalline powder annealed for 12 hrs, and the phase mapping in Fig. 5 (b) distinguished (Fe, Cr)-rich FCC matrix and (Al, Ti)-rich BCC precipitates. The EBSD results confirm that the dark contrast phase in Fig. 4(a) and (b) is (Al, Ti)-rich phase and the light contrast matrix is (Fe, Cr)-rich phase. The phase mapping image in EBSD shown in Fig. 5(c) presents the segregation of Al, along with Ti in the annealed group (i) powder. The FCC matrix plus BCC precipitate heterogeneous structure demonstrated in this study of

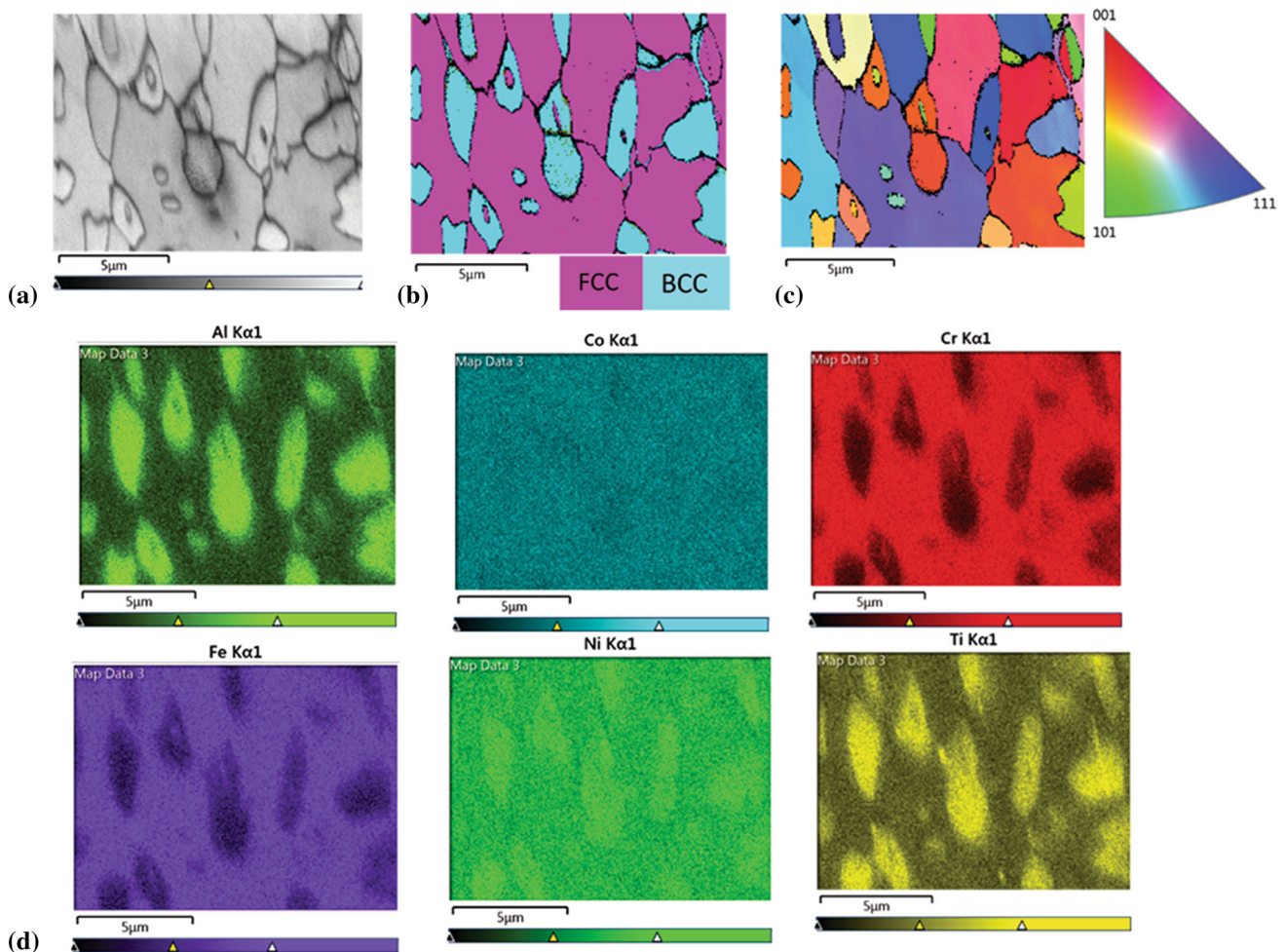


Fig. 5 EBSD results of group (i) powder after annealed at 1000 °C for 12 hrs, including (a) band contrast, (b) phase mapping image, showing the phase fraction occupied by FCC and BCC, (c) inverse pole figure and (d) elemental mapping of all six elements

$\text{Al}_{0.5}\text{CoCrFeNi}_2\text{Ti}_{0.5}$ alloy provides a great blend of ductility and strength critical in the industrial application of this alloy (Ref 7, 8, 29, 30). Due to the high-entropy effect, $\text{Al}_{0.5}\text{CoCrFeNi}_2\text{Ti}_{0.5}$ alloy is devoid of brittle intermetallic compounds and therefore expected to have enhanced mechanical properties (Ref 31).

Enhanced mechanical properties in HEAs are highly desirable in the industrial applications such as in surface coatings (Ref 8, 13, 14, 17, 18). The as-atomized and annealed $\text{Al}_{0.5}\text{CoCrFeNi}_2\text{Ti}_{0.5}$ powders were analyzed to determine their hardness using a nanoindenter. Figure 6(a) shows the SPM image of the 12-hr annealed group (i) powder in cross-sectional surface scanned by the nanoindenter diamond tip with a normal force of $3\mu\text{N}$. Similar normal force of $3\mu\text{N}$ was applied in nanoindentation to ascertain the difference of hardness for the annealed and as-atomized powders. An increase of over 20% increase in hardness for the 12-hr annealed powder compared to the as-atomized powders attributed to the

precipitation strengthening. The hardness of as-atomized group (i) powder was 5.329 GPa, while the annealed powder was 6.561 GPa. The difference in hardness between the as-atomized and the annealed powders is not large, which implies that the properties of $\text{Al}_{0.5}\text{CoCrFeNi}_2\text{Ti}_{0.5}$ alloy do not deteriorate with high temperature. The hardness values for 12-hr annealed powder in the FCC matrix, and the BCC precipitates is shown in Fig. 6(b). The dark-contrast phases, which have been analyzed in XRD, SEM and EBSD as BCC precipitates, had high hardness compared to the light-contrast FCC matrix. In Fig. 6(a) SPM, image indicates that harder BCC precipitates have smaller indentation marks compared to the FCC matrix due to the degree of resistance to indenter penetration resulting in the difference in hardness. The addition of titanium to $\text{Al}_{0.5}\text{CoCrFeNi}_2$ leads to heterogeneous structure, which strengthens the alloy with BCC precipitates without sacrificing the ductility (Ref 11–14).

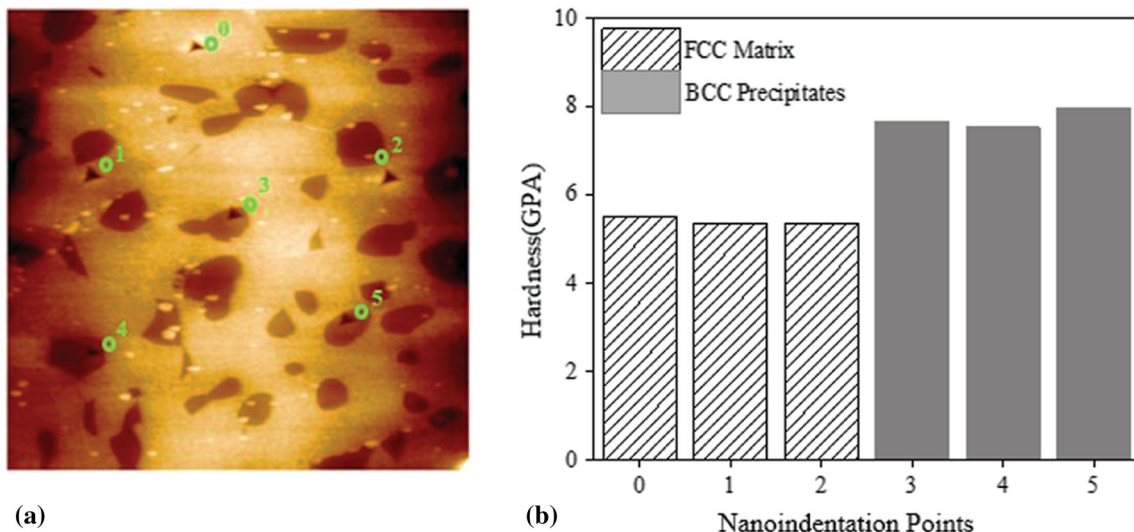


Fig. 6 (a) SPM image and (b) indentation results of hardness of $Al_{0.5}CoCrFeNi_2Ti_{0.5}$ group (i) powder after annealing at 1000 °C for 12 hrs. Point Nos. 0 to 5 are associated with the marks in of indented

group (i) powder annealed for 12 hrs. The indentation was done on the matrix (FCC) and the precipitate (BCC)

Characteristics of $Al_{0.5}CoCrFeNi_2Ti_{0.5}$ Plasma-Sprayed Coatings

The parameters shown in Table 1 were used to investigate the properties of the coatings performed on carbon steel substrates. Moreover, the comparison was made on the influence of group (i) and (ii) sized powders on the coating microstructure and mechanical properties so as to understand the particle size effect. The current and the argon gas flow rate were varied, while the secondary gas hydrogen was kept constant during the plasma-sprayed process so as to study the influence of input power on the plasma-sprayed coating properties. Whereas the secondary hydrogen gas was used to suppress oxidation, the Ar gas complements current as spraying power (Ref 7, 8). The phase constitution of the coatings prepared using the group (i) had FCC phase as shown in the XRD pattern in Fig. 7, which was similar to coatings prepared using the group (ii) powder having FCC (Ref 8). Consequently, the plasma-sprayed coatings produced using group (i) powders maintained a minor BCC peak at 64.733 ° (200) similar to the annealed powders. Under the different spraying parameters, plasma-sprayed coatings would not achieve complete annealed status as the annealed powders due to inadequate time and energy to transform. Nonetheless, the energy was enough to promote ordering within a short time for coatings prepared using group (i) powders, which enabled to change metastable BCC peak along (100) into ordered BCC at 30.591 °. Coatings prepared with group (ii) powder kept the status of as-obtained powders as presented in Fig. 3, as the bigger particle size would not get enough time and energy to be annealed. From Fig. 7, it is demonstrated

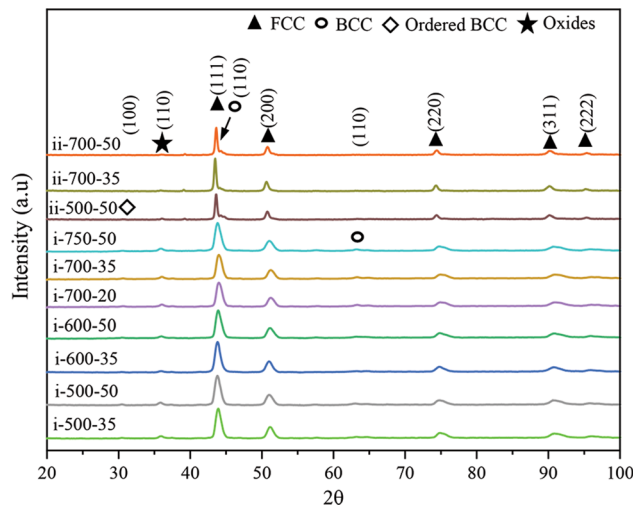


Fig. 7 XRD analysis of the plasma-sprayed samples in different parameters

that the properties of plasma-sprayed coatings can be varied with plasma power and the size of powder particles involved (Ref 7, 8, 19).

The microstructure under different spraying parameters for the plasma-sprayed coatings using group (i) and group (ii) powders was investigated using SEM to observe their morphology. The cross-sectional images of the samples with the lowest (500-35) and the highest (750-50) spraying parameters are shown in Fig. 8(a), (b), and (c), respectively, alongside the point EDS elemental analysis. The evidence of unmelted powders is attributed to low plasma power, which significantly affects the mechanical properties of the coating. The high power applied in plasma-

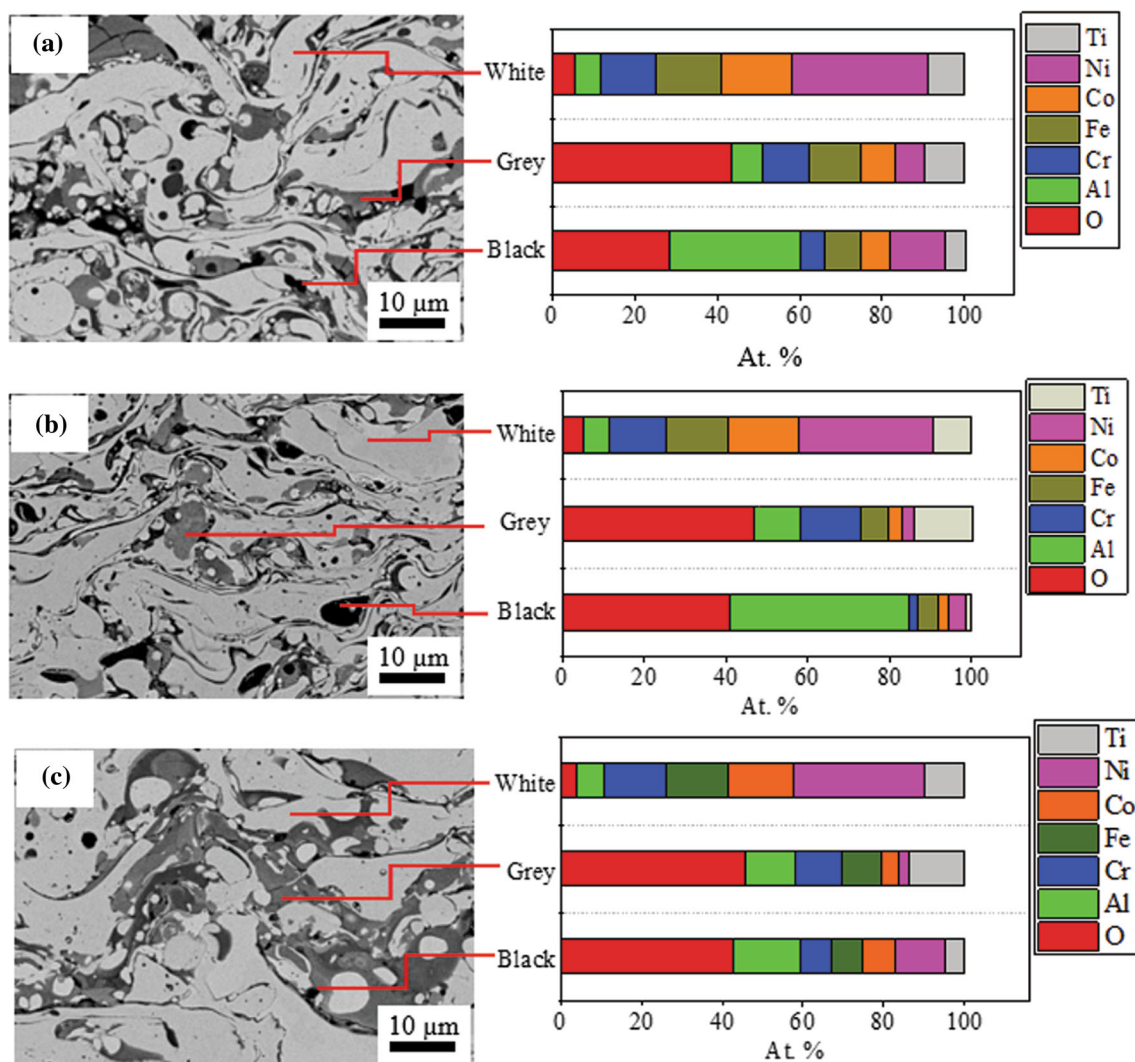


Fig. 8 Cross-sectional image of plasma-sprayed coatings and the phase compositions identified via point EDS of group (i) (a) 500-50 and (b) 750-50 and (c) group (ii)

sprayed coating as depicted in Fig. 8(b) resulted in a complete melting and a continuous layer of splats with reduced porosity, voids and denser. The presence of small-sized unmelted powders in Fig. 8(b) is ascribed to rapid cooling before they are deposited on the substrate (Ref 7, 8, 14). The group (ii) coatings sprayed at high plasma power (750-50) shown in Fig. 8(c) demonstrated incomplete melting of the powders. This observation is due to large powder particles, which require more time to heat and melt. In all the coatings, three regions were observable, which were characterized via the point EDS analysis. The black region was aluminum-rich oxide, which could be Al_2O_3 as the atomic percentages of aluminum and O₂ from the EDS analysis are close to that of Al_2O_3 . The dark gray region is Al-Cr-Ti-rich oxide, while the light gray (white)-colored region is a multicomponent HEA depleted of aluminum. The Al-Cr-Ti-rich oxide is widespread through the

coatings and could be the oxide phase observed in XRD analysis in Fig. 7 at 36.05° . The microstructure of the plasma-sprayed coatings, which varies with the plasma power, has a direct impact on mechanical properties such as, hardness, ductility and wear resistance (Ref 7, 8, 14, 32).

The hardness of sprayed samples increased proportionally with increasing plasma power as shown in Fig. 9. The difference in hardness for plasma-sprayed coatings prepared using group (i) powder marked between i-500-35 and i-750-50 is due to the different microstructures as discussed above. Additionally, the coatings prepared using group (ii) powders had lower hardness values, an observation which was reported in previous studies (Ref 7, 8). The group (ii) powders are comparatively larger than group (i) making it difficult to completely melt and form dense continuous coating with better bonding (Ref 7, 8). The group (ii)

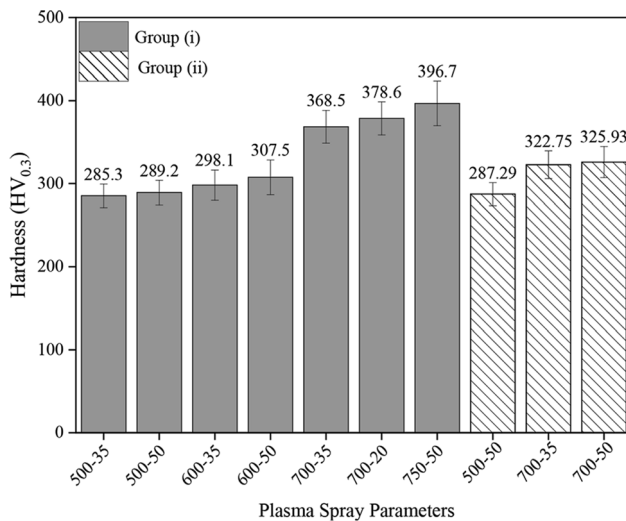


Fig. 9 The hardness of $\text{Al}_{0.5}\text{CoCrFeNi}_2\text{Ti}_{0.5}$ plasma-sprayed coatings with different spraying parameters

coatings are also observed to have more oxides than the group (i) coatings at high plasma powers. The higher plasma spraying power raises the working temperature and ultimately leads to a dense and continuous coating (Ref 7, 8, 14, 19). There is better bonding due to less defects for coatings formed under high plasma power, resulting in high hardness values. Whereas the hardness increased from 285.3 to 396.7 HV as the current was increased from 500 to 750 A, the effect of increasing the Ar gas flow rate was minimal. When compared with the previous research on $\text{Al}_{0.5}\text{CoCrFeNi}_2$ (Ref 8), the addition of titanium significantly increased the hardness from 279.1 to 396.7 HV. Moreover, it is expected that as plasma power is increased, denser coating will form since higher power will promote complete melting of the powders beyond the 750 A (Ref 7, 8, 33). The oxides and voids in the plasma coatings greatly affect the mechanical properties as the process is performed in atmospheric environment. Nonetheless, the improved mechanical properties due to the addition of titanium compared to $\text{Al}_{0.5}\text{CoCrFeNi}_2$ (Ref 8) make $\text{Al}_{0.5}\text{CoCrFeNi}_2\text{Ti}_{0.5}$ suitable for industrial use in applications that require rapidly developed thick porous coatings. In plasma-sprayed coatings, the microstructure that ultimately impacts mechanical properties can be adjusted with plasma power depending on the application.

Characterization of the $\text{Al}_{0.5}\text{CoCrFeNi}_2\text{Ti}_{0.5}$ Cold-Sprayed Coatings

The group (i) powder was chosen to study the properties of cold-sprayed coatings on carbon steel and AA 6061 substrates. The cross-sectional SEM images of the cold-sprayed AA6061 and carbon steel substrates in Fig. 10(a) and (b), respectively, demonstrate a relatively

clean, defect-free, microstructure having few cracks, compared to the plasma-sprayed coatings. As a result of particles impact on the substrate at supersonic speeds and cold spray process being a solid-state process, densification of the powder particles occurred.

A good interface between the substrate and the coating, discontinuous cracks across the coating parallel to the interface and the lack of oxide stringers between the splats are some of observable features in Fig. 10(a) and (b) of the cold-sprayed coatings. Such cracks might be detrimental to the mechanical properties of the coatings. The intersplat cracks may have resulted from the severe plastic deformation generated at the edge of cold-sprayed particles. The edges of the particle-substrate and particle-particle are prone to plastic shear deformation due to severe impact, which results in jetting. Multiple-particle deposition at high-velocity impact during CS process crumbles the jetting morphology to form a folded structure as shown, marked with arrows in Fig. 10(a) (Ref 16, 21, 34)

The XRD results displayed in Fig. 11(a) show that the cold-sprayed $\text{Al}_{0.5}\text{CoCrFeNi}_2\text{Ti}_{0.5}$ coatings on carbon steel and AA 6061 substrates had FCC phase with minor metastable BCC. Analysis of the XRD spectra of the cold-sprayed coatings with the respective group (i) powders indicates that there is no phase transformation that took place during the cold-sprayed process. Although the metastable state of the raw powder was retained, it is evident that XRD spectra peak broadening occurred in the cold-sprayed coatings when compared to the feedstock powders XRD spectra in Fig. 3. Researchers (Ref 35) established that cold spray process retains the status of the feedstock powders as no melting is involved. Peak broadening can be attributed to either refinement of grain sizes or a strain effect (Ref 36, 37).

High atomic strain effect often caused by residual stresses due to melting of feedstock powders in plasma-sprayed and HVOF coatings leads to the first possibility of peak broadening. The cold-sprayed coatings experienced much lower temperatures, which could not cause annealing of feedstock powders, and therefore, strain effect by residual stresses from high temperatures was not taken into consideration. Nonetheless, the impact of high velocities of powder particles, which leads to densification of the coatings, causes compressive stresses due to continuous ‘hammering’ action similar to shot peening. These compressive stresses may lead to a high strain effect causing peak broadening. Additionally, the cold-sprayed coatings peak broadening may be attributed to decrease in particles sizes, as they are refined by the severe plastic deformation. XRD peak broadening is influenced by small grain sizes at low angles and micro-strain effect at high angles (Ref 38, 39).

Whereas plasma coatings rely on plasma power, which can be adjusted to melt powders and create a better

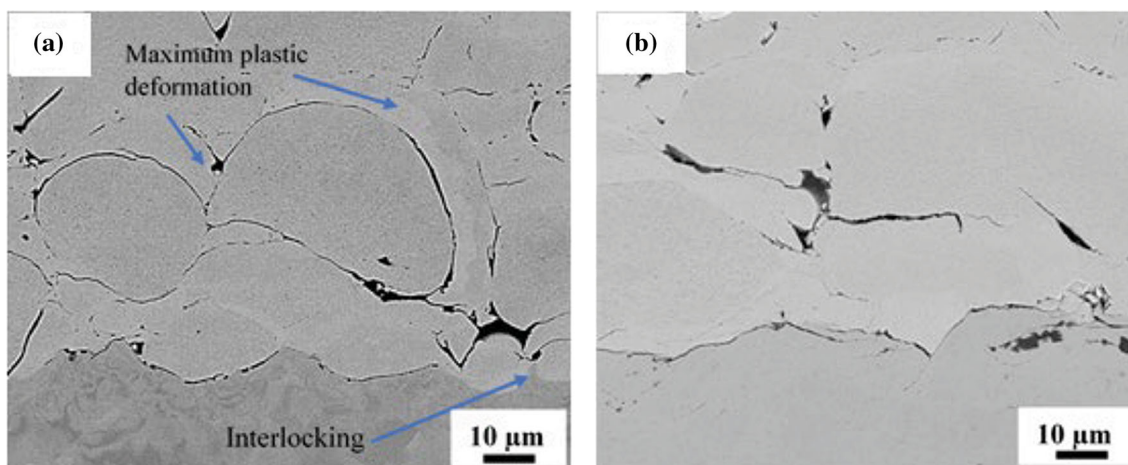


Fig. 10 Cross-sectional SEM image of (a) AA 6061, (b) carbon steel substrate cold-sprayed HEA coatings with group (i) powder

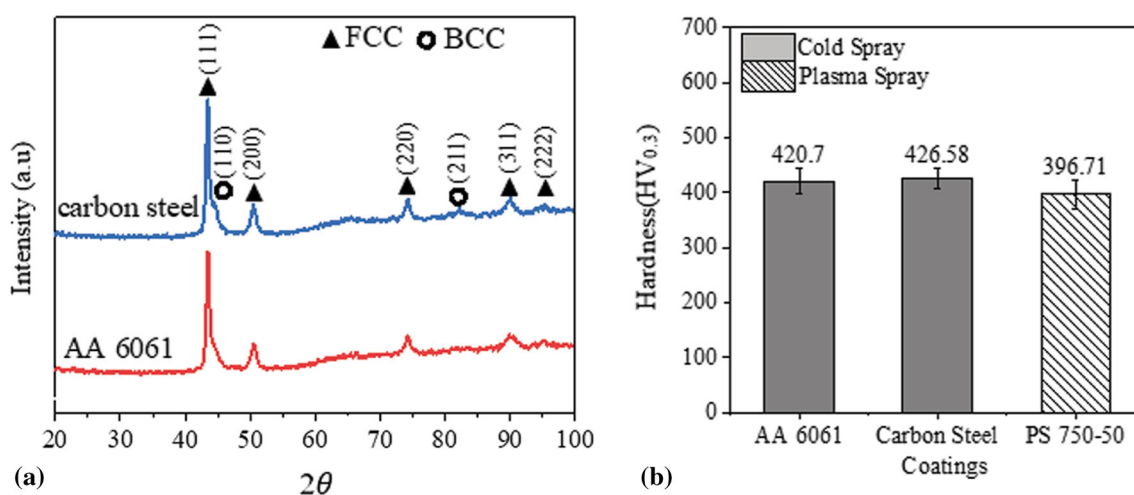


Fig. 11 (a) XRD analysis of cold-sprayed carbon steel substrate and 6061 aluminum alloy and (b) Vickers microhardness of the plasma- and cold-sprayed coatings

bonding, the cold spray coatings solely depend on kinetic energy of the particles creating an impact on the substrate and consequently deforming to create a strong bond (Ref 22, 40). The flattening and interlocking of the splats due to cold forging under forward pressure are caused by severe plastic deformation of the powder particles (Ref 16, 21). In addition, the localized deformation causes shear instability at the particle boundaries, which has been established by researchers (Ref 41, 42) to be effective in creating effective mechanical bonding between adjacent splats. Figure 10(a) shows the comparison of the hardness between the cold-sprayed coatings and the plasma-sprayed coatings. The cold spray coatings have higher hardness as they largely retain the status of the raw group (i) powders. Figure 10(b) shows the BSE image of the cold-sprayed coatings on AA 6061 and demonstrates the presence of slightly deformed $\text{Al}_{0.5}\text{CoCrFeNi}_2\text{Ti}_{0.5}$ powder particles, with the narrow interfacial surrounded by intersplat cracks.

At the particle-substrate and particle-particle interfaces, the mechanical locking caused by localized severe plastic deformation is observable in Fig. 11(a). This process minimizes defects that are common in high-temperature deposition processes and ultimately improves the mechanical properties of the cold-sprayed coatings (Ref 21). Similar observations were made by Li et al. (Ref 41). The adhesion of particles in cold spray process is mainly due to kinetic energy upon impact rather than thermal energy as compared to plasma process where melting is involved (Ref 23, 26). Therefore, there is no melting and the particles remain in a solid state during the entire deposition process in cold-sprayed coatings (Ref 22).

The values of pull-off adhesive bonding strength test on cold-sprayed $\text{Al}_{0.5}\text{CoCrFeNi}_2\text{Ti}_{0.5}$ AA 6061 substrates showed that the coating averaged the bond strength of 69.84 MPa. The observation on the AA 6061 showed that the coating was intact and the failure occurred at the

adhesive, which has a maximum bonding strength of 70 MPa. This was approximately 20% higher than that of 57.26 MPa on carbon steel. Investigators (Ref 40) attributed significant substrate deformation to have enhanced mechanical interlocking in cold-sprayed AA 6082 where they reported a bond strength of 57.26 MPa. Furthermore, the researchers (Ref 40, 43) found that the failure occurred at the coating substrate interface. Although the interparticle bonding in $\text{Al}_{0.5}\text{CoCrFeNi}_2\text{Ti}_{0.5}$ deposit was good, a lack of adequate mechanical interlocking due to poor deformation of the carbon substrate may have contributed to lower bond strength. The integrity of the interface between the AA 6061 substrate and the $\text{Al}_{0.5}\text{CoCrFeNi}_2\text{Ti}_{0.5}$ coating as shown in Fig. 11(b) exhibits sufficiently great bonding. Figure 11(b) displays evidence of significant deformation in AA 6061 substrate, which resulted in mechanical interlocking of the cold-sprayed powders facilitating a well-bonded interface region. However, the cold-sprayed coatings on carbon steel substrate shown in Fig. 11(c) was less deformed and had no observable interlocking features. The hardness values measured for both substrates support this observation, as carbon steel substrate of 152.41 Hv and AA 6061 of 120.56 Hv. Because of high deformation resulting in large portions of mechanically interlocked regions and metallurgical bonding, AA 6061 performed high adhesive bonding strength compared to the cold-sprayed coatings on carbon steel (Ref 25, 40).

Conclusion

Through the numerous experiments that have been conducted in this study, it is evident that the addition of titanium to $\text{Al}_{0.5}\text{CoCrFeNi}_2$ has greatly improved the mechanical properties of the coatings. Both coatings retained the phases and properties of the as-atomized powders. Minor ordered BCC phase was observed in the group (i) plasma-sprayed coatings, while the group (ii) plasma-sprayed and group (i) cold-sprayed coatings kept the status of the as-obtained crystal structures. Precipitation strengthening by the addition of titanium to $\text{Al}_{0.5}\text{CoCrFeNi}_2$ enhanced the mechanical properties of annealed powders and the coatings. High hardness values were realized in the plasma-sprayed coatings of $\text{Al}_{0.5}\text{CoCrFeNi}_2\text{Ti}_{0.5}$ group (i) compared to group (ii) powder. Microstructure and mechanical properties of plasma-spray coatings can be adjusted with increasing plasma power. Consequently, it was established that phase constitution was maintained as plasma power was increased, which implies that the gas-atomized as-obtained powders have good phase stability. Additionally, the cold-sprayed coatings had higher mechanical properties and can significantly improve the carbon steel and AA 6061 application in aggressive environments.

Acknowledgment Authors acknowledge the support from the Ministry of Science and Technology of Taiwan under Project No. 107-2218-E-011-017 and the support by the Research Center for Intelligent Medical Devices, Ming Chi University of Technology. This work was financially supported by the “High Entropy Materials Center” from The Featured Areas Research Center Program within the framework of the Higher Education Sprout Project by the Ministry of Education (MOE) and from Project MOST 109-2634-F-007-024 by the Ministry of Science and Technology (MOST) in Taiwan. Thanks for Plus Metal Tech., Co. supporting in conducting plasma and cold spraying processes.

Author Contribution Rotich Sammy Kiplangat was involved in writing—original draft, investigation. Tzu-Tang Lin performed writing—review & editing and investigation. Ngetich Gilbert Kipkirui contributed to investigation and data curation. Shih-Hsun Chen did supervision, methodology and resources.

Conflict of interest The authors declare that they have no known competing financial interests or personal relationships that could have appeared to influence the work reported in this paper.

References

1. J. Yeh, S. Chen, J. Gan, S. Lin and T. Chin, Formation of Simple Crystal Structures in Cu-Co-Ni-Cr-Al-Fe-Ti-V Alloys with Multiprincipal Metallic, *Elements*, 2004, **2010**(35), p 2533-2536.
2. Y. Zhang, T.T. Zuo, Z. Tang, M.C. Gao, K.A. Dahmen, P.K. Liaw and Z.P. Lu, Microstructures and Properties of High-Entropy Alloys, *Prog. Mater. Sci.*, 2014, **61**, p 1-93. <https://doi.org/10.1016/j.pmatsci.2013.10.001>
3. A. Manzoni, H. Daoud, R. Völkl, U. Glatzel and N. Wanderka, Phase Separation in Equiatomic AlCoCrFeNi High-Entropy Alloy, *Ultramicroscopy*, 2013, **132**, p 212-215. <https://doi.org/10.1016/j.ultramic.2012.12.015>
4. P.D. Niu, R.D. Li, T.C. Yuan, S.Y. Zhu, C. Chen, M.B. Wang and L. Huang, Microstructures and Properties of an Equimolar AlCoCrFeNi High Entropy Alloy Printed by Selective Laser Melting, *Intermetallics*, 2019, **104**, p 24-32. <https://doi.org/10.1016/j.intermet.2018.10.018>
5. V. Shivam, J. Basu, V.K. Pandey, Y. Shadangi and N.K. Mukhopadhyay, Alloying Behaviour, Thermal Stability and Phase Evolution in Quinary AlCoCrFeNi High Entropy Alloy, *Adv. Powder Technol.*, 2018, **29**(9), p 2221-2230. <https://doi.org/10.1016/j.apt.2018.06.006>
6. Q.H. Li, T.M. Yue, Z.N. Guo and X. Lin, Microstructure and Corrosion Properties of AlCoCrFeNi High Entropy Alloy Coatings Deposited on AISI 1045 Steel by the Electrospark Process, *Metall. Mater. Trans. A*, 2013, **44**(4), p 1767-1778. <https://doi.org/10.1007/s11661-012-1535-4>
7. K.-C. Cheng, J.-H. Chen, S. Stadler and S.-H. Chen, Properties of Atomized AlCoCrFeNi High-Entropy Alloy Powders and Their Phase-Adjustable Coatings Prepared via Plasma Spray Process, *Appl. Surf. Sci.*, 2019, **478**, p 478-486. <https://doi.org/10.1016/j.apsusc.2019.01.203>
8. J.-T. Liang, K.-C. Cheng, Y.-C. Chen, S.-M. Chiu, C. Chiu, J.-W. Lee and S.-H. Chen, Comparisons of Plasma-Sprayed and Sputtering $\text{Al}_{0.5}\text{CoCrFeNi}_2$ High-Entropy Alloy Coatings, *Surf. Coatings Technol.*, 2020, **403**, p 126411. <https://doi.org/10.1016/j.surfcoat.2020.126411>
9. W.-R. Wang, W.-L. Wang, S.-C. Wang, Y.-C. Tsai, C.-H. Lai and J.-W. Yeh, Effects of Al Addition on the Microstructure and Mechanical Property of $\text{Al}_x\text{CoCrFeNi}$ High-Entropy Alloys,

- Intermetallics*, 2012, **26**, p 44-51. <https://doi.org/10.1016/j.intermet.2012.03.005>
10. M. López Ríos, P.P. Socorro Perdomo, I. Voiculescu, V. Geanta, V. Crăciun, I. Boerasu, and J.C. Mirza Rosca, Effects of Nickel Content on the Microstructure, Microhardness and Corrosion Behavior of High-Entropy AlCoCrFeNi Alloys, *Sci. Rep.*, 2020, **10**(1), 21119
 11. M. Wu, K. Chen, Z. Xu and D.Y. Li, Effect of Ti Addition on the Sliding Wear Behavior of AlCrFeCoNi High-Entropy Alloy, *Wear*, 2020, **462-463**, 203493. <https://doi.org/10.1016/j.wear.2020.203493>
 12. G.-S. Ham, Y.-K. Kim, Y.S. Na and K.-A. Lee, Effect of Ti Addition on the Microstructure and High-Temperature Oxidation Property of AlCoCrFeNi High-Entropy Alloy, *Met. Mater. Int.*, 2021, **27**(1), p 156-165. <https://doi.org/10.1007/s12540-020-00708-7>
 13. Z. Xu, D.Y. Li and D.L. Chen, Effect of Ti on the Wear Behavior of AlCoCrFeNi High-Entropy Alloy during Unidirectional and Bi-Directional Sliding Wear Processes, *Wear*, 2021, **476**, 203650. <https://doi.org/10.1016/j.wear.2021.203650>
 14. M. Löbel, T. Lindner, T. Mehner and T. Lampke, Microstructure and Wear Resistance of AlCoCrFeNiTi High-Entropy Alloy Coatings Produced by HVOF, *Coatings*, 2017, **7**(9), p 144.
 15. M. Chuang, M. Tsai, W. Wang, S. Lin and J. Yeh, Microstructure and Wear Behavior of AlxCo1.5CrFeNi1.5Ti High-Entropy Alloys, *Acta Mater.*, 2011, **59**, p 6308-6317.
 16. G.P. León, V.E. Lamberti, R.D. Seals, T.M. Abu-Lebdeh and S.A. Hamoush, Gas Atomization of Molten Metal: Part I. Numerical Modeling Conception, *Am. J. Eng. Appl. Sci.*, 2016, **9**(2), p 303-322. <https://doi.org/10.3844/ajeassp.2016.303.322>
 17. J. Lehtonen, Y. Ge, N. Ciftci, O. Heczko, V. Uhlenwinkel and S.-P. Hannula, Phase Structures of Gas Atomized Equiatomic CrFeNiMn High Entropy Alloy Powder, *J. Alloys Compd.*, 2020, **827**, p 154142. <https://doi.org/10.1016/j.jallcom.2020.154142>
 18. J. Liu, H. Liu, P. Chen and J. Hao, Microstructural Characterization and Corrosion Behaviour of AlCoCrFeNiTi_x High-Entropy Alloy Coatings Fabricated by Laser Cladding, *Surf. Coatings Technol.*, 2019, **361**, p 63-74. <https://doi.org/10.1016/j.surfcoat.2019.01.044>
 19. A.S.M. Ang, C.C. Berndt, M.L. Sesso, A. Anupam, P. S, R.S. Kottada, and B.S. Murty, Plasma-Sprayed High Entropy Alloys: Microstructure and Properties of AlCoCrFeNi and MnCoCrFeNi, *Metall. Mater. Trans. A Phys. Metall. Mater. Sci.*, 2015, **46**(2), 791-800.
 20. F. Gärtner, T. Stoltenhoff, T. Schmidt and H. Kreye, The Cold Spray Process and Its Potential for Industrial Applications, *J. Therm. Spray Technol.*, 2006, **15**(2), p 223-232. <https://doi.org/10.1361/105996306X108110>
 21. A. Anupam, S. Kumar, N.M. Chavan, B.S. Murty and R.S. Kottada, First Report on Cold-Sprayed AlCoCrFeNi High-Entropy Alloy and Its Isothermal Oxidation, *J. Mater. Res.*, 2019, **34**(5), p 796-806. <https://doi.org/10.1557/jmr.2019.38>
 22. D.V. Hushchuk, A.I. Yurkova, V.V. Cherniavsky, I.I. Bilyk and S.O. Nakonechnyy, Nanostructured AlNiCoFeCrTi High-Entropy Coating Formed by Cold Spray, *Appl. Nanosci.*, 2020, **10**(12), p 4879-4890. <https://doi.org/10.1007/s13204-020-01364-4>
 23. S. Yin, W. Li, B. Song, X. Yan, M. Kuang, Y. Xu, K. Wen and R. Lupoi, Deposition of FeCoNiCrMn High Entropy Alloy (HEA) Coating via Cold Spraying, *J. Mater. Sci. Technol.*, 2019, **35**(6), p 1003-1007. <https://doi.org/10.1016/j.jmst.2018.12.015>
 24. Y. Liang, B. Shi, X. Yang, J. Zhang and X. Meng, Microstructure and Nano-Mechanical Property of Cold Spray Co-Base Refractory Alloy Coating, *Acta Metall. Sin. English Lett.*, 2011, **24**(3), p 190-194.
 25. C. Huang, W. Li, Y. Xie, M.-P. Planche, H. Liao and G. Montavon, Effect of Substrate Type on Deposition Behavior and Wear Performance of Ni-Coated Graphite/Al Composite Coatings Deposited by Cold Spraying, *J. Mater. Sci. Technol.*, 2017, **33**(4), p 338-346. <https://doi.org/10.1016/j.jmst.2016.11.016>
 26. S. Yin, P. Cavaliere, B. Aldwell, R. Jenkins, H. Liao, W. Li and R. Lupoi, Cold Spray Additive Manufacturing and Repair: Fundamentals and Applications, *Addit. Manuf.*, 2018, **21**, p 628-650. <https://doi.org/10.1016/j.addma.2018.04.017>
 27. L. Ajdelsztajn, B. Jodoin, G.E. Kim and J.M. Schoenung, Cold Spray Deposition of Nanocrystalline Aluminum Alloys, *Metall. Mater. Trans. A*, 2005, **36**(11), p 3263-3263. <https://doi.org/10.1007/s11661-005-0099-y>
 28. Q. Cao, G. Huang, L. Ma and L. Xing, Comparison of a Cold-sprayed and Plasma-sprayed Fe₂₅Cr₂₀Mo₁Si Amorphous Alloy Coatings on 40Cr Substrates, *Mater. Corros.*, 2020, **71**(11), p 1872-1884. <https://doi.org/10.1002/maco.202011558>
 29. J. Liang, K. Cheng and S. Chen, Effect of Heat Treatment on the Phase Evolution and Mechanical Properties of Atomized AlCoCrFeNi High-Entropy Alloy Powders, *J. Alloys Compd.*, 2019, **803**, p 484-490. <https://doi.org/10.1016/j.jallcom.2019.06.301>
 30. S.-M. Chiu, T.-T. Lin, R.K. Sammy, N.G. Kipkirui, Y.-Q. Lin, J.-T. Liang and S.-H. Chen, Investigation of Phase Constitution and Stability of Gas-Atomized Al_{0.5}CoCrFeNi₂ High-Entropy Alloy Powders, *Mater. Chem. Phys.*, 2022, **275**, p 125194. <https://doi.org/10.1016/j.matchemphys.2021.125194>
 31. S. Jiang, Z. Lin, H. Xu and Y. Sun, Studies on the Microstructure and Properties of AlxCoCrFeNiTi_{1-x} High Entropy Alloys, *J. Alloys Compd.*, 2018, **741**, p 826-833. <https://doi.org/10.1016/j.jallcom.2018.01.247>
 32. E. Garcia, H. Lee and S. Sampath, Phase and Microstructure Evolution in Plasma Sprayed Yb₂Si₂O₇ Coatings, *J. Eur. Ceram. Soc.*, 2019, **39**(4), p 1477-1486. <https://doi.org/10.1016/j.jeurceramsoc.2018.11.018>
 33. J. Luo, N. Shi, Y.-Z. Xing, C. Jiang and Y. Chen, Effect of Arc Power on the Wear and High-Temperature Oxidation Resistances of Plasma-Sprayed Fe-Based Amorphous Coatings, *High Temp. Mater. Process.*, 2019, **2019**(38), p 639-646. <https://doi.org/10.1515/htmp-2019-0003>
 34. C. Lee and J. Kim, Microstructure of Kinetic Spray Coatings: A Review, *J. Therm. Spray Technol.*, 2015, **24**(4), p 592-610. <https://doi.org/10.1007/s11666-015-0223-5>
 35. H.-T. Wang, C.-J. Li, G.-J. Yang, C.-X. Li, Q. Zhang and W.-Y. Li, Microstructural Characterization of Cold-Sprayed Nanostructured FeAl Intermetallic Compound Coating and Its Ball-Milled Feedstock Powders, *J. Therm. Spray Technol.*, 2007, **16**(5-6), p 669-676. <https://doi.org/10.1007/s11666-007-9089-5>
 36. A. Chaudhuri, Y. Raghupathy, D. Srinivasan, S. Suwas and C. Srivastava, Microstructural Evolution of Cold-Sprayed Inconel 625 Superalloy Coatings on Low Alloy Steel Substrate, *Acta Mater.*, 2017, **129**, p 11-25. <https://doi.org/10.1016/j.actamat.2017.02.070>
 37. K. Kim, S. Kuroda, M. Watanabe, R. Huang, H. Fukunuma and H. Katanoda, Comparison of Oxidation and Microstructure of Warm-Sprayed and Cold-Sprayed Titanium Coatings, *J. Therm. Spray Technol.*, 2012, **21**(June), p 550-560. <https://doi.org/10.1007/s11666-011-9703-4>
 38. H.-T. Wang, C.-J. Li, G.-J. Yang and C.-X. Li, Effect of Heat Treatment on the Microstructure and Property of Cold-Sprayed Nanostructured FeAl/Al₂O₃ Intermetallic Composite Coating, *Vacuum*, 2008, **83**(1), p 146-152. <https://doi.org/10.1016/j.vacuum.2008.03.094>
 39. L. Shaw, H. Luo, J. Villegas and D. Miracle, Thermal Stability of Nanostructured Al₉₃Fe₃Cr₂Ti₂ Alloys Prepared via Mechanical Alloying, *Acta Mater.*, 2003, **51**(9), p 2647-2663.
 40. T. Hussain, D.G. McCartney and P.H. Shipway, Bonding between Aluminium and Copper in Cold Spraying: Story of

- Asymmetry, *Mater. Sci. Technol.*, 2012, **28**(12), p 1371-1378. <https://doi.org/10.1179/1743284712Y.0000000051>
41. Y. Li, X. Wang, S. Yin and S. Xu, Influence of Particle Initial Temperature on High Velocity Impact Process in Cold Spraying, *Procedia Environ. Sci.*, 2011, **2012**(12(Icese)), p 298-304. <https://doi.org/10.1016/j.proenv.2012.01.281>
42. M.R. Rokni, S.R. Nutt, C.A. Widener, V.K. Champagne and R.H. Hrabec, Review of Relationship Between Particle Deformation, Coating Microstructure, and Properties in High-Pressure Cold Spray, *J. Therm. Spray Technol.*, 2017, **26**(6), p 1308-1355. <https://doi.org/10.1007/s11666-017-0575-0>
43. R. Drehmann, T. Grund, T. Lampke, B. Wielage, C. Wüstefeld, M. Motylenko and D. Rafaja, Essential Factors Influencing the Bonding Strength of Cold-Sprayed Aluminum Coatings on Ceramic Substrates, *J. Therm. Spray Technol.*, 2018, **27**(3), p 446-455. <https://doi.org/10.1007/s11666-018-0688-0>

Publisher's Note Springer Nature remains neutral with regard to jurisdictional claims in published maps and institutional affiliations.